

Supporting information

**Elucidating The Charge Storage Mechanism of High-Performance Vertical
Graphene Cathodes for Zinc-Ion Hybrid Supercapacitors**

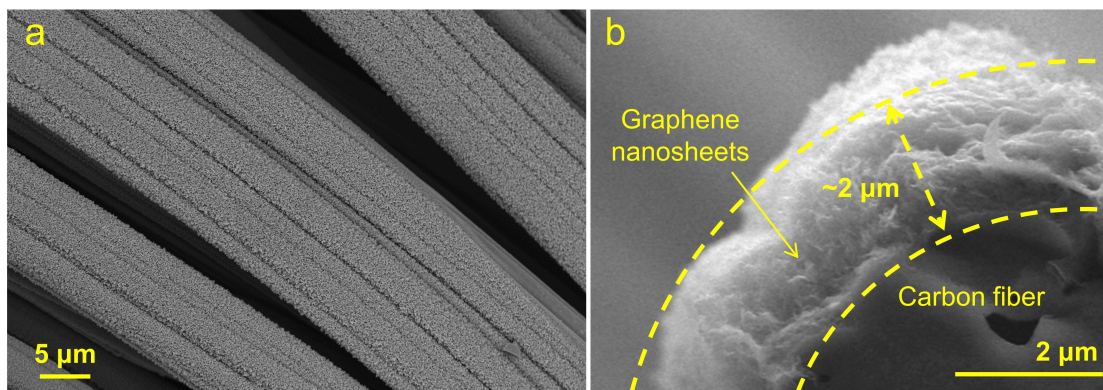


Fig. S1 (a) Surface and (b) cross-sectional SEM images of the VGN sample.

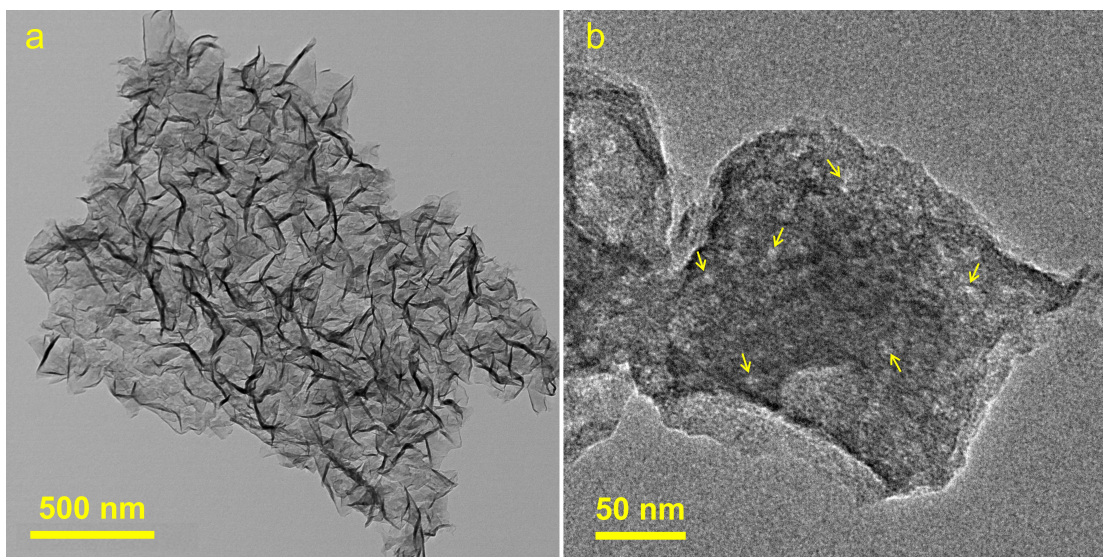


Fig. S2 TEM images of the graphene nanosheets in the A-VGN sample. Abundant pores can be observed on the graphene nanosheets, as pointed out by arrows in (b).

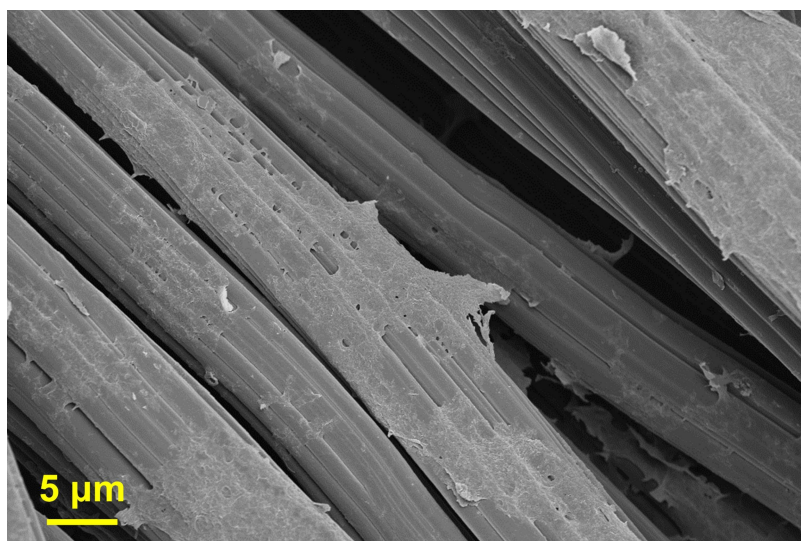


Fig. S3 SEM image of the DGN sample.

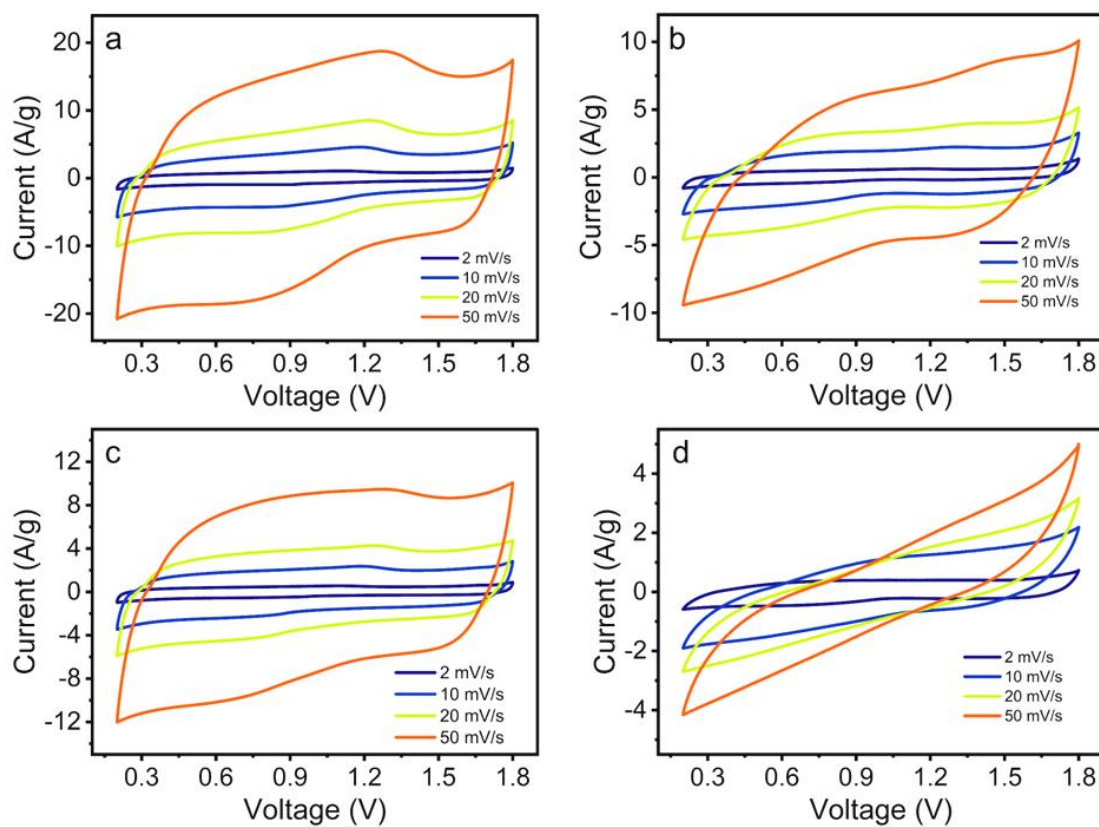


Fig. S4 CV curves of the (a) A-VGN, (b) VGN, (c) A-DGN and (d) DGN cathode-based ZHSs at different scan rates.

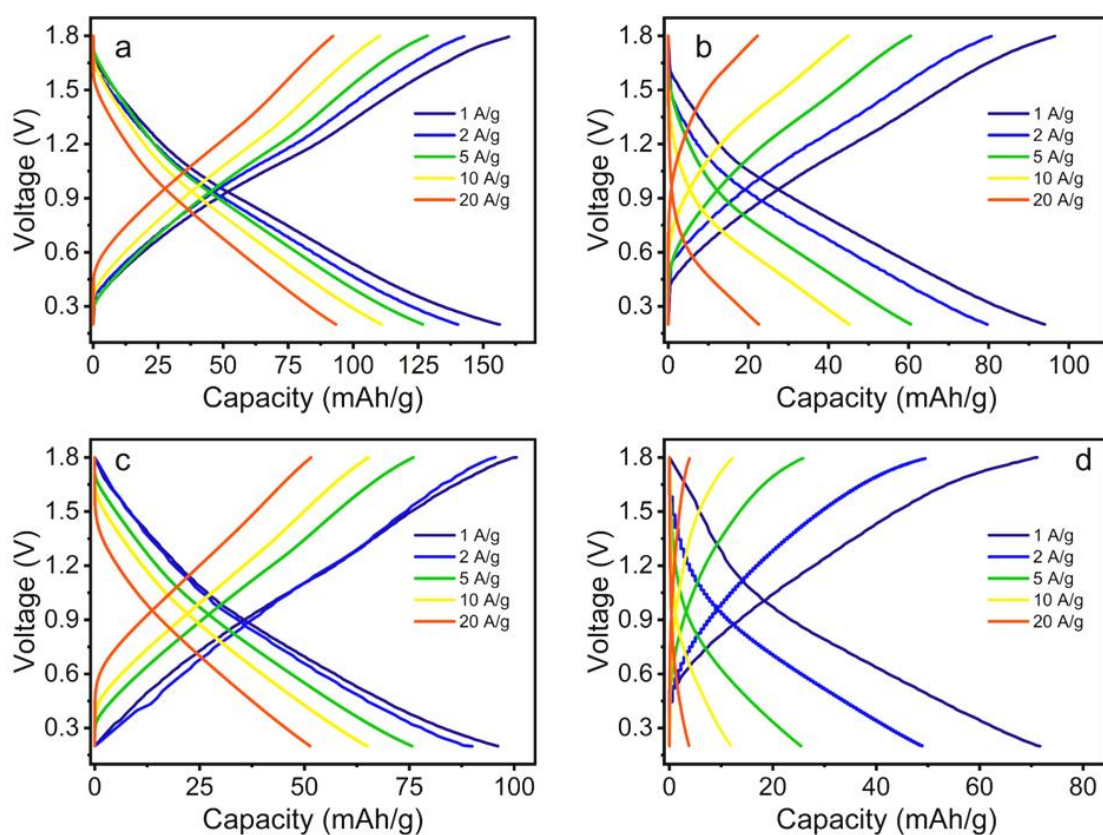


Fig. S5 GCD profiles of the (a) A-VGN, (b) VGN, (c) A-DGN and (d) DGN cathode-based ZHSs at different current densities.

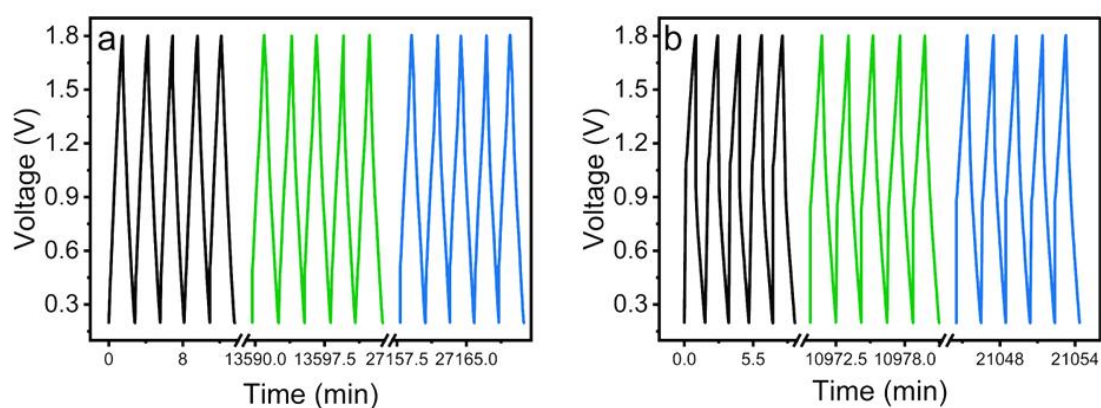


Fig. S6 The first, middle and last 5 cycles of GCD curves during long-term cycling tests of the (a) A-VGN and (b) A-DGN cathode-based ZHSs.

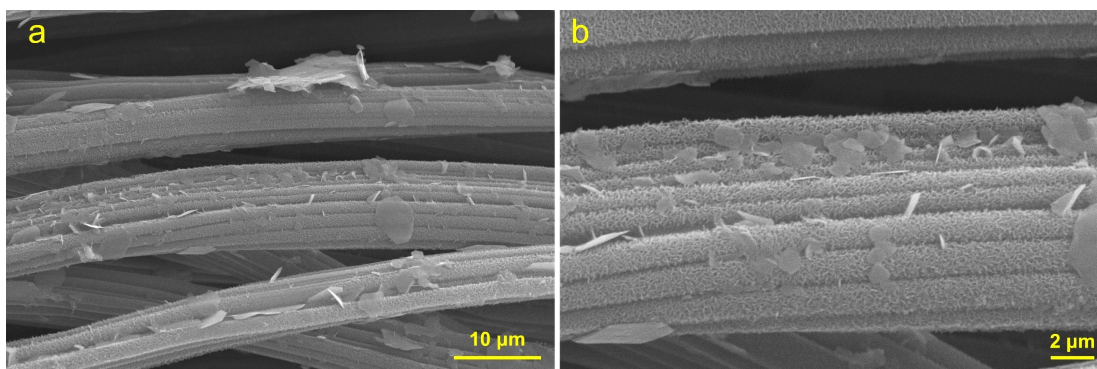
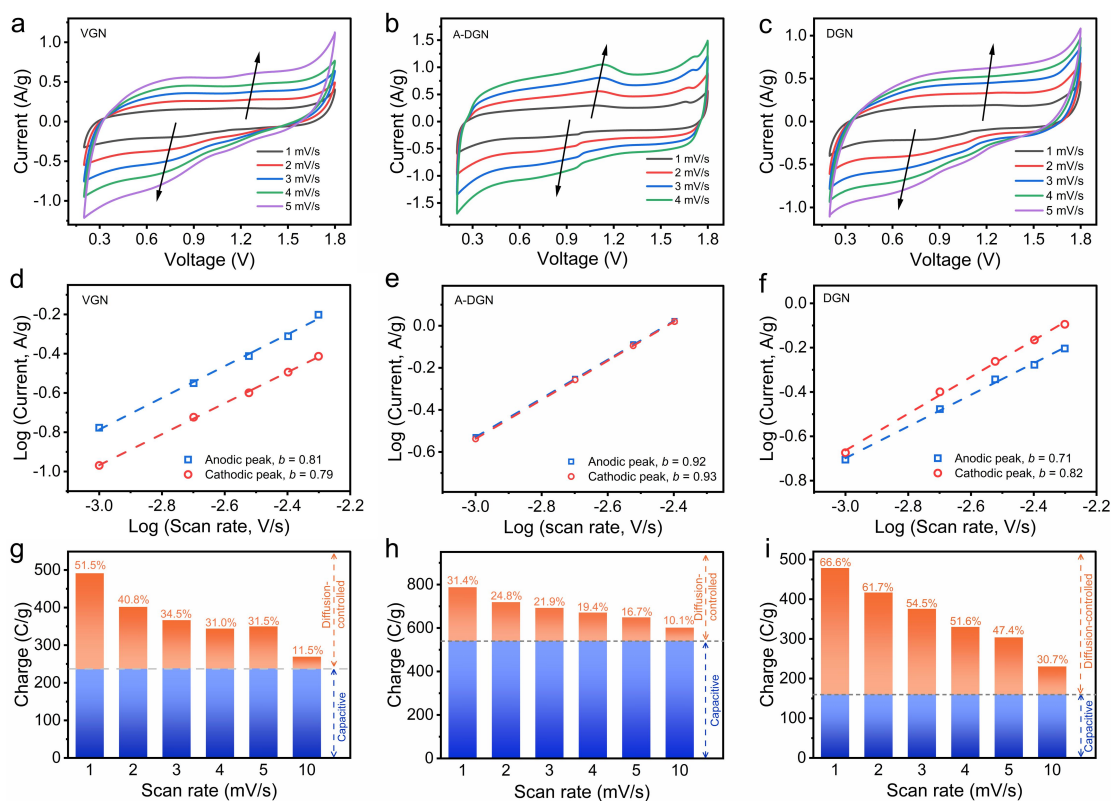


Fig. S7 SEM images of the A-VGN cathode after cycling test. Since the cathode after cycling is not at fully charged state, $\text{Zn}_4\text{SO}_4(\text{OH})_6 \cdot 4\text{H}_2\text{O}$ flakes are reasonable to be observed (as discussed in Fig. 5). Despite this, the vertical graphene array structure in the A-VGN cathode keep well during the long-term cycling test.



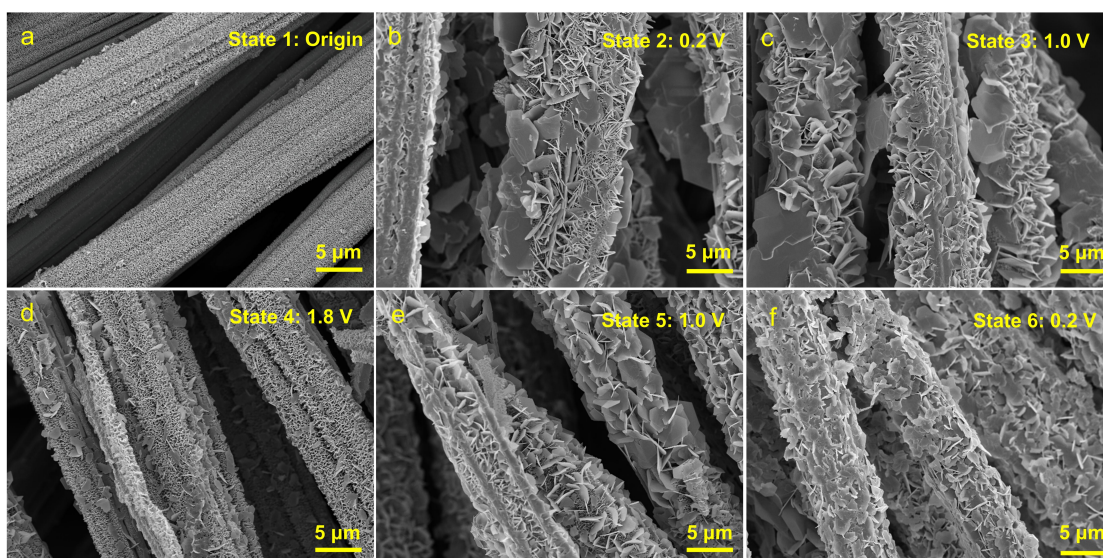


Fig. S9 SEM images of the A-VGN cathode at different charge/discharge states.

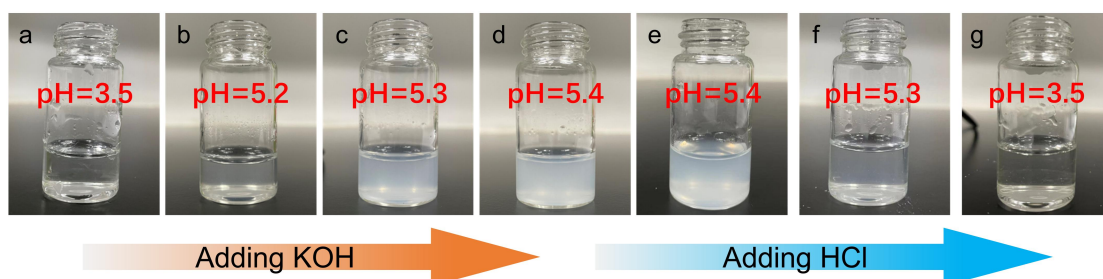


Fig. S10 The formation/dissolution of BZS precipitate in 2 M ZnSO_4 aqueous with different pH values. The pH of the electrolyte was adjusted by adding 0.1 M KOH or HCl aqueous solution, and these pH values given in the images were determined using a pH testing meter. The results indicate that BZS precipitation becomes obvious when the pH value exceeds about 5.2 (note that BZS can be regarded as a pH buffer since its formation consumes OH^-), and BZS precipitate dissolves with decreasing pH value of electrolytes.

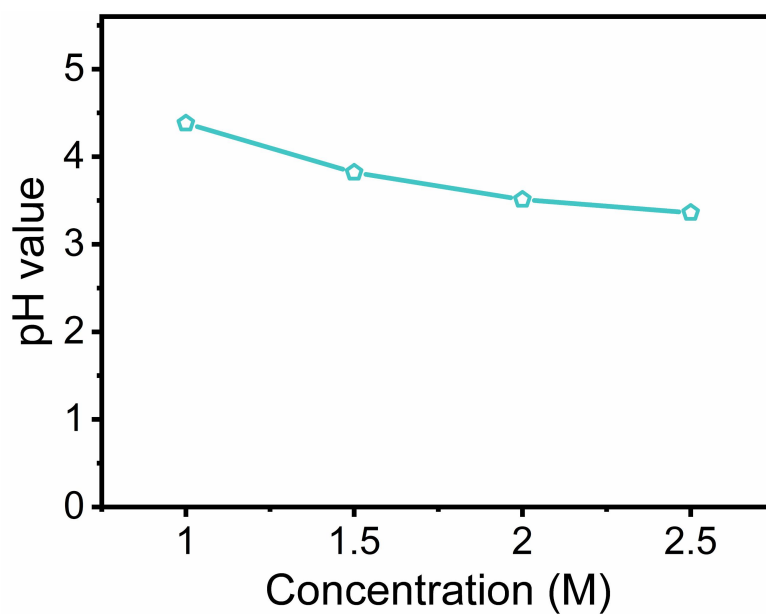


Fig. S11 The pH value of ZnSO₄ aqueous solutions with various concentrations. The pH decreases with increasing concentration for ZnSO₄ aqueous solutions.

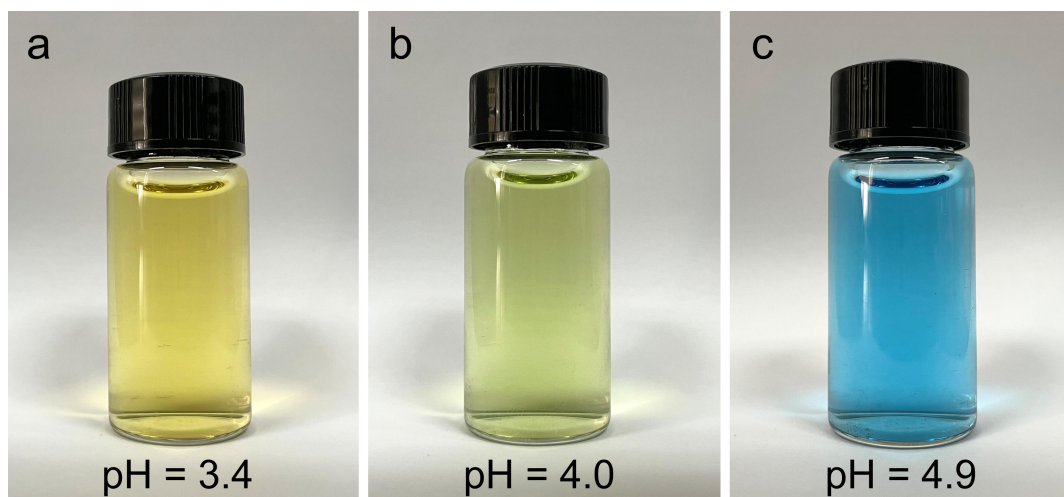


Fig. S12 The color of bromocresol green aqueous solutions with different pH values. Volume fraction of the bromocresol green in the aqueous solutions is ~0.6%.

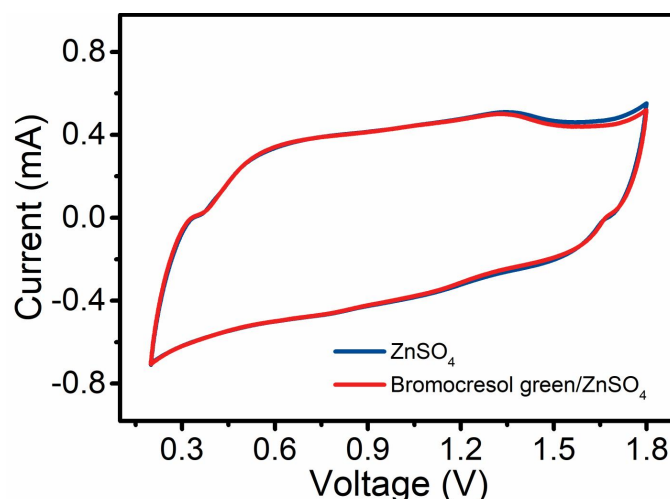


Fig. S13 CV curves at 10 mV/s of the A-VGN cathode-based ZHSs in pure ZnSO_4 and bromocresol green (0.6% in volume)/ ZnSO_4 aqueous electrolytes.

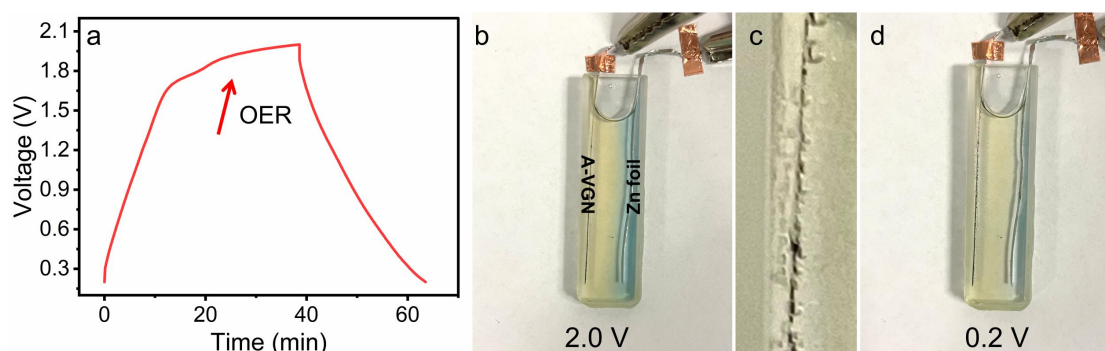


Fig. S14 (a) GCD curve of the A-VGN cathode-based ZHS with an operating voltage range of 0.2-2.0 V; (b-d) digital photos of the electrolyte when the ZHS is changed to 2.0 V and then discharged to 0.2 V. According to the GCD curve, OER occurs when the operating voltage of ZHS exceeds 1.8 V. Meanwhile, bubbles are observed on the A-VGN cathode, as displayed in (c). Since OER dramatically and irreversibly decreases the pH of the electrolyte around the A-VGN cathode, the dark yellow color almost occupies the most area of the electrolyte when the ZHS is charged to 2.0 V and does not disappear when the ZHS is then discharged to 0.2 V. In one word, if OER occurs, electrolyte color will not reversibly change between blue and yellow during charge/discharge processes of ZHSs.

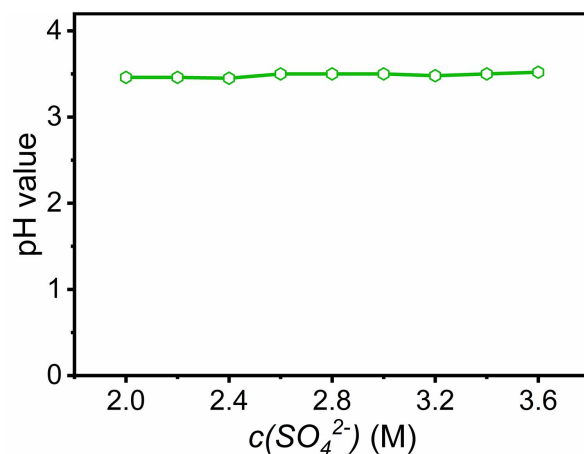


Fig. S15 pH values of $\text{ZnSO}_4/\text{Na}_2\text{SO}_4$ aqueous solutions with different SO_4^{2-} concentrations.

Note: To evaluate the effect of SO_4^{2-} concentration on the pH of ZnSO_4 electrolyte, we prepared $\text{ZnSO}_4/\text{Na}_2\text{SO}_4$ mixture solutions in which the concentration of ZnSO_4 is always 2 M while the concentration of Na_2SO_4 changes from 0 to 1.6 M. In such a case, Zn^{2+} concentration is constant (excluding the effect of Zn^{2+} concentration on the pH value of corresponding solutions), and SO_4^{2-} concentration varies from 2.0 to 3.6 M. These mixture solutions show almost same pH values (3.49 ± 0.02 , Fig. S15). Therefore, the concentration variation of SO_4^{2-} is not the reason causing notable pH change at the carbon cathode-electrolyte interface during charge/discharge processes.

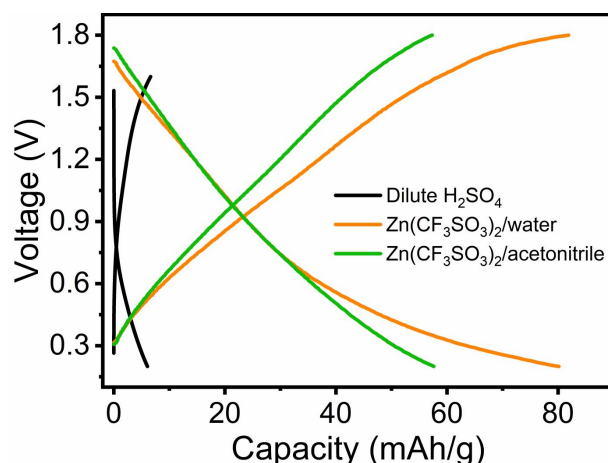


Fig. S16 GCD profiles at 0.2 A/g of the activated carbon//Zn ZHSs with dilute H₂SO₄ aqueous electrolyte (pH=3.5), 1 M Zn(CF₃SO₃)₂ aqueous electrolyte and 1 M Zn(CF₃SO₃)₂/acetonitrile electrolyte.

Note: Electrochemical properties of an activated carbon cathode in different electrolytes including H⁺-free 1 M Zn(CF₃SO₃)₂/acetonitrile electrolyte, Zn²⁺-free dilute H₂SO₄ aqueous electrolyte (pH=3.5, close to that of 2 M ZnSO₄ aqueous electrolyte) and Zn²⁺/H⁺ co-existed 1 M Zn(CF₃SO₃)₂ aqueous electrolyte were investigated. Since ZnSO₄ cannot dissolve in acetonitrile solvent, we choose Zn(CF₃SO₃)₂ as the solute in the above electrolytes. As displayed in Fig. S16, at a current density of 0.2 A/g, capacity of the carbon cathode is 6, 58 and 80 mAh/g, respectively, in dilute H₂SO₄ aqueous electrolyte, Zn(CF₃SO₃)₂/acetonitrile electrolyte and Zn(CF₃SO₃)₂ aqueous electrolyte, strongly demonstrating the Zn²⁺ charge storage mechanism in ZHS system again.

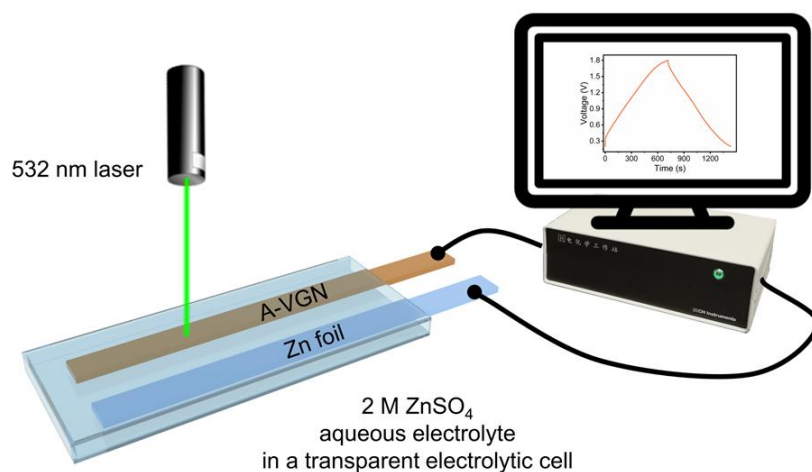


Fig. S17 Schematic diagram of *in-operando* Raman test of the A-VGN cathode. The ZHS was charged/discharged through an electrochemical workstation, and at the same time, Raman spectra of the A-VGN cathode were continuously recorded.

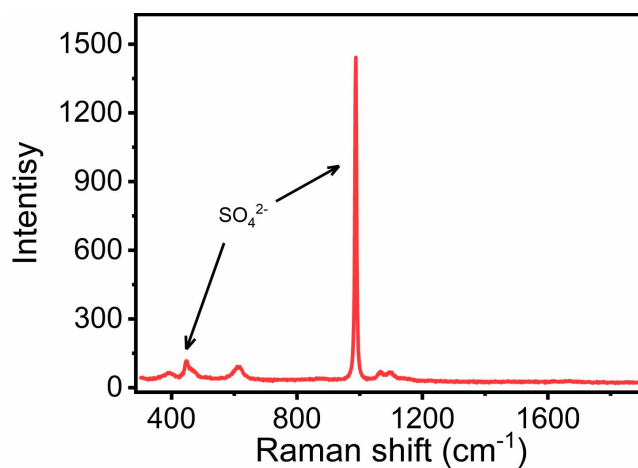


Fig. S18 Raman spectra of $\text{ZnSO}_4 \cdot 7\text{H}_2\text{O}$ powder. The characteristic peaks at 445 and 986 cm^{-1} belong to SO_4^{2-} .^[S1-S2]

Table S1. Specific surface area and pore structure of the samples

Sample	Specific surface area (m ² /g)	Pore volume (cm ³ /g)	Pore volume ratio	
			Micropore	Meso/Macropore
VGN	945	0.454	96%	4%
A-VGN	1664	0.800	93%	7%
DGN	887	0.391	99%	1%
A-DGN	2454	1.098	96%	4%

Table S2. Summary of electrochemical performance of carbon cathodes for ZHSs

Carbon cathodes	Energy density (Mass loading)	Power density	Capacity (mAh/g)	Capacity retention after cycling	Ref. (Publish year)
A-VGN	165 Wh/kg (10.3 mg/cm²)	15 kW/kg (70 Wh/kg)	246 (0.2 A/g) 94 (20 A/g)	97.4%-10000 cycles (5 A/g)	This work
N-OPCNF	98 Wh/kg (4.5 mg/cm ²)	8 kW/kg (50 Wh/kg)	136 (0.1 A/g) 68 (20 A/g)	99.2%-200000 cycles (40 A/g)	S3 (2022)
rGO	48 Wh/kg (5.5 mg/cm ²)	-	123 (0.5 A/g) 65 (20 A/g)	75%-10000 cycles (10 A/g)	S4 (2022)
3D-PG	86 Wh/kg (N) ^a	17 kW/kg (44 Wh/kg)	102 (0.1 A/g) 77 (5 A/g)	85%-30000 cycles (5 A/g)	S5 (2022)
N-carbon nanosheets	198 Wh/kg (1.1 mg/cm ²)	-	211 (0.5 A/g) 115 (10 A/g)	118.2%-10000 cycles (5 A/g)	S6 (2022)
Bone glue-derived carbon	168 Wh/kg (1 mg/cm ²)	61 kW/kg (45 Wh/kg)	257 (0.5 A/g) 150 (10 A/g)	100%-10000 cycles (5 A/g)	S7 (2021)
N/P-carbon nanosheets	81 Wh/kg (2.1 mg/cm ²)	13 kW/kg (40 Wh/kg)	103 (0.1 A/g) 53 (20 A/g)	100%-10000 cycles (5 A/g)	S8 (2021)
O/N-CF	127 Wh/kg (N)	15 kW/kg (36 Wh/kg)	156 (0.1 A/g) 79 (20 A/g)	93%-6000 cycles (20 A/g)	S9 (2021)
O/P-CNF	98 Wh/kg (4.4 mg/cm ²)	10 kW/kg (19 Wh/kg)	136 (0.1 A/g) 39 (20 A/g)	81%-50000 cycles (5 A/g)	S10 (2021)
Pencil shavings -derived carbon	147 Wh/kg (2 mg/cm ²)	16 kW/kg (65 Wh/kg)	184 (0.2 A/g) 82 (20 A/g)	92.2%-10000 cycles (10 A/g)	S11 (2020)
Mesoporous hollow carbon spheres	129 Wh/kg (1 mg/cm ²)	14 kW/kg (37 Wh/kg)	174 (0.1 A/g) 97 (10 A/g)	100%-10000 cycles (1 A/g)	S12 (2020)
P/B-AC	169 Wh/kg (N)	20 kW/kg (67 Wh/kg)	169 (0.5 A/g) 84 (10 A/g)	88%-30000 cycles (10 A/g)	S13 (2020)
Ordered and compact porous carbon	112 Wh/kg (10 mg/cm ²)	24 kW/kg (81 Wh/kg)	114 (0.1 A/g) 80 (20 A/g)	100%-20000 cycles (5 A/g)	S14 (2020)
2D porous carbon nanoflakes	142 Wh/kg (1.2 mg/cm ²)	68 kW/kg (15.4 Wh/kg)	178 (0.5 A/g) 57 (20 A/g)	90%-10000 cycles (10 A/g)	S15 (2020)
Layered B/N-carbon	98 Wh/kg (2 mg/cm ²)	12 kW/kg (19 Wh/kg)	128 (0.5 A/g) 43 (20 A/g)	81.3%-6500 cycles (5 A/g)	S16 (2019)
Activated rGO	106 Wh/kg (N)	31 kW/kg (50 Wh/kg)	88 (0.5 A/g)	93%-80000 cycles (8 A/g)	S17 (2019)
AC	84 Wh/kg (0.7 mg/cm ²)	15 kW/kg (30 Wh/kg)	121 (0.1 A/g) 41 (20 A/g)	91%-10000 cycles (1 A/g)	S18 (2018)

^a “N” means that the mass loading is not mentioned in the literature.

Note: We can see that our A-VGN cathode is superior to most of currently-reported carbon cathodes in electrochemical performance (*e.g.*, capacity and energy density). Even for a few reported carbon cathodes whose energy density and capacity are comparable to those of the A-VGN cathode, their good electrochemical properties are achieved at a low mass loading of 1-2 mg/cm². Moreover, the A-VGN cathode is a free-standing electrode without binder, conductive additives and extra current collectors (*e.g.*, metal foils). By contrast, many previously-reported carbon cathodes are composed of carbon active materials, binder, conductive additives and metal current collectors. If the mass of these inactive components (*i.e.*, polymer binder, conductive additives and current collectors) is also taken into account, the calculated capacity and energy density of these carbon cathodes will decrease dramatically.

References

- [S1] A. C. Hayes, P. Kruus, W. A. Adams, Raman spectroscopic study of aqueous (NH₄)₂SO₄ and ZnSO₄ solutions, *J. Solution Chem.* 13 (1984) 61-75.
- [S2] A. J. Locke, W. N. Martens, R. L. Frost, Natural halotrichites-an EDX and Raman spectroscopic study, *J. Raman Spectrosc.* 38 (2007) 1429-1435.
- [S3] H. He, J. Lian, C. Chen, Q. Xiong, C. Li, M. Zhang, Enabling multi-chemisorption sites on carbon nanofibers cathodes by an in-situ exfoliation strategy for high-performance Zn-ion hybrid capacitors, *Nano-Micro Lett.* 14 (2022) 106.
- [S4] H. Xu, W. He, Z. Li, J. Chi, J. Jiang, K. Huang, S. Li, G. Sun, H. Dou, X. Zhang, Revisiting charge storage mechanism of reduced graphene oxide in zinc ion hybrid capacitor beyond the contribution of oxygen-containing groups, *Adv. Funct. Mater.* 32 (2022) 2111131.
- [S5] X. Xu, X. Zhao, Z. Yang, Q. Li, B. Jian, N. Li, C. Zheng, W. Lv, High-density three-dimensional graphene cathode with a tailored pore structure for high volumetric capacity zinc-ion storage, *Carbon* 186 (2022) 624-631.
- [S6] P. Shang, M. Liu, Y. Mei, Y. Liu, L. Wu, Y. Dong, Z. Zhao, J. Qiu, Urea-mediated monoliths made of nitrogen-enriched mesoporous carbon nanosheets for

high-performance aqueous zinc ion hybrid capacitors, *Small* 18 (2022) 2108057.

[S7] W. Fan, J. Ding, J. Ding, Y. Zheng, W. Song, J. Lin, C. Xiao, C. Zhong, H. Wang, W. Hu, Identifying heteroatomic and defective sites in carbon with dual-ion adsorption capability for high energy and power zinc ion capacitor, *Nano-Micro Lett.* 13 (2021) 59.

[S8] H. Zhang, Z. Chen, Y. Zhang, Z. Ma, Y. Zhang, L. Bai, L. Sun, Boosting Zn-ion adsorption in cross-linked N/P co-incorporated porous carbon nanosheets for the zinc-ion hybrid capacitor, *J. Mater. Chem. A* 9 (2021) 16565-16574.

[S9] Y. Li, W. Yang, W. Yang, Z. Wang, J. Rong, G. Wang, C. Xu, F. Kang, L. Dong, Towards high-energy and anti-self-discharge Zn-ion hybrid supercapacitors with new understanding of the electrochemistry, *Nano-Micro Lett.* 13 (2021) 95.

[S10] H. He, J. Lian, C. Chen, Q. Xiong, M. Zhang, Super hydrophilic carbon fiber film for freestanding and flexible cathodes of zinc-ion hybrid supercapacitors, *Chem.Eng. J.* 421 (2021) 129786.

[S11] Z. Li, D. Chen, Y. An, C. Chen, L. Wu, Z. Chen, Y. Sun, X. Zhang, Flexible and anti-freezing quasi-solid-state zinc ion hybrid supercapacitors based on pencil shavings derived porous carbon, *Energy Storage Mater.* 28 (2020) 307-314.

[S12] P. Liu, W. Liu, Y. Huang, P. Li, J. Yan, K. Liu, Mesoporous hollow carbon spheres boosted, integrated high performance aqueous Zn-ion energy storage, *Energy Storage Mater.* 25 (2020) 858-865.

[S13] Y. G. Lee, G. H. An, Synergistic effects of phosphorus and boron co-incorporated activated carbon for ultrafast zinc-ion hybrid supercapacitors, *ACS Appl. Mater. Interfaces* 12 (2020) 41342-41349.

[S14] H. Ma, H. Chen, M. Wu, F. Chi, F. Liu, J. Bai, H. Cheng, C. Li, L. Qu, Maximization of spatial charge density: an approach to ultrahigh energy density of capacitive charge storage, *Angew. Chem. Int. Ed.* 59 (2020) 14541-14549.

[S15] Z. Pan, Z. Lu, L. Xu, D. Wang, A robust 2D porous carbon nanoflake cathode for high energy-power density Zn-ion hybrid supercapacitor applications, *Appl. Surf. Sci.* 510 (2020) 145384.

[S16] Y. Lu, Z. Li, Z. Bai, H. Mi, C. Ji, H. Pang, C. Yu, J. Qiu, High energy-power Zn-ion hybrid supercapacitors enabled by layered B/N co-doped carbon cathode, *Nano Energy* 66 (2019) 104132.

[S17] S. Wu, Y. Chen, T. Jiao, J. Zhou, J. Cheng, B. Liu, S. Yang, K. Zhang, W. Zhang,

An aqueous Zn-ion hybrid supercapacitor with high energy density and ultrastability up to 80,000 cycles, *Adv. Energy Mater.* 9 (2019) 1902915.

[S18] L. Dong, X. Ma, Y. Li, L. Zhao, W. Liu, J. Cheng, C. Xu, B. Li, Q. H. Yang, F. Kang, Extremely safe, high-rate and ultralong-life zinc-ion hybrid supercapacitors, *Energy Storage Mater.* 13 (2018) 96-102.